Biochar

ORIGINAL RESEARCH

Open Access

Development of hazelnut shell-derived biochar to support a bifunctional MoCo electrocatalyst for HER/OER in alkaline medium

Jaime Ñanculeo[1], Teresa Andreu[2], Ignasi Sirés[2], Andrés Ramírez[3], Mara Cea[4,5], Benjamín Nahuelcura[1], Gerson Valenzuela[4], Karla Garrido-Miranda[5] and María Eugenia González[4,5*]

Abstract

Hydrogen evolution reaction (HER) and oxygen evolution reaction (OER), the two concurrent reactions for the electrolytic production of green H_2, require low-cost and sustainable electrocatalysts for their scale-up, as for example non-noble metals and carbonaceous structures with high surface area. Our hypothesis is that the activated-doped biochar decorated with Mo and Co provides high porosity and active site dispersion, enhancing HER and OER kinetics with low overpotentials and high stability in an alkaline medium. Here, a bifunctional Mo/Co electrocatalyst supported on N-doped biochar obtained from hazelnut shells has been developed, thus valorizing an agro-industrial residue of major importance in Chile. The activated biochar matrix, with interconnected hierarchical pores, offered a high surface area of 1102 $m^2\ g^{-1}$ and $I_D/I_G = 1.08$ graphitization, while N-doping was observed by XPS, with the formation of N-pyridinic and N-graphitic functionalities that improved the catalytic performance. The addition of metals to the substrate allowed the formation of bimetallic Mo/Co active sites (Co_6Mo_6C), increasing the graphitization degree and improved the growth of these bimetallic sites. The electrocatalytic performance in the presence of the metals was good, revealing low overpotentials for HER (0.257 V) and OER (0.370 V) with low Tafel slopes (51 and 59 mV dec^{-1}, respectively) under alkaline conditions, also improving the electron transfer and stability.

Highlights

- The activation and doping of biochar (BC) was carried out using a one-step methodology, facilitating its production.
- N-doped BC from hazelnut shells exhibited a surface area of 1102 $m^2\ g^{-1}$ and an I_D/I_G ratio of 1.08, being further used for the BC-Mo/Co synthesis.
- The combination of Mo and Co was more effective than their single use, improving the electrocatalytic performance.

Keywords Biochar, Electrocatalysts, Green H_2, Bifunctional

*Correspondence:
María Eugenia González
mariaeugenia.gonzalez@ufrontera.cl
Full list of author information is available at the end of the article

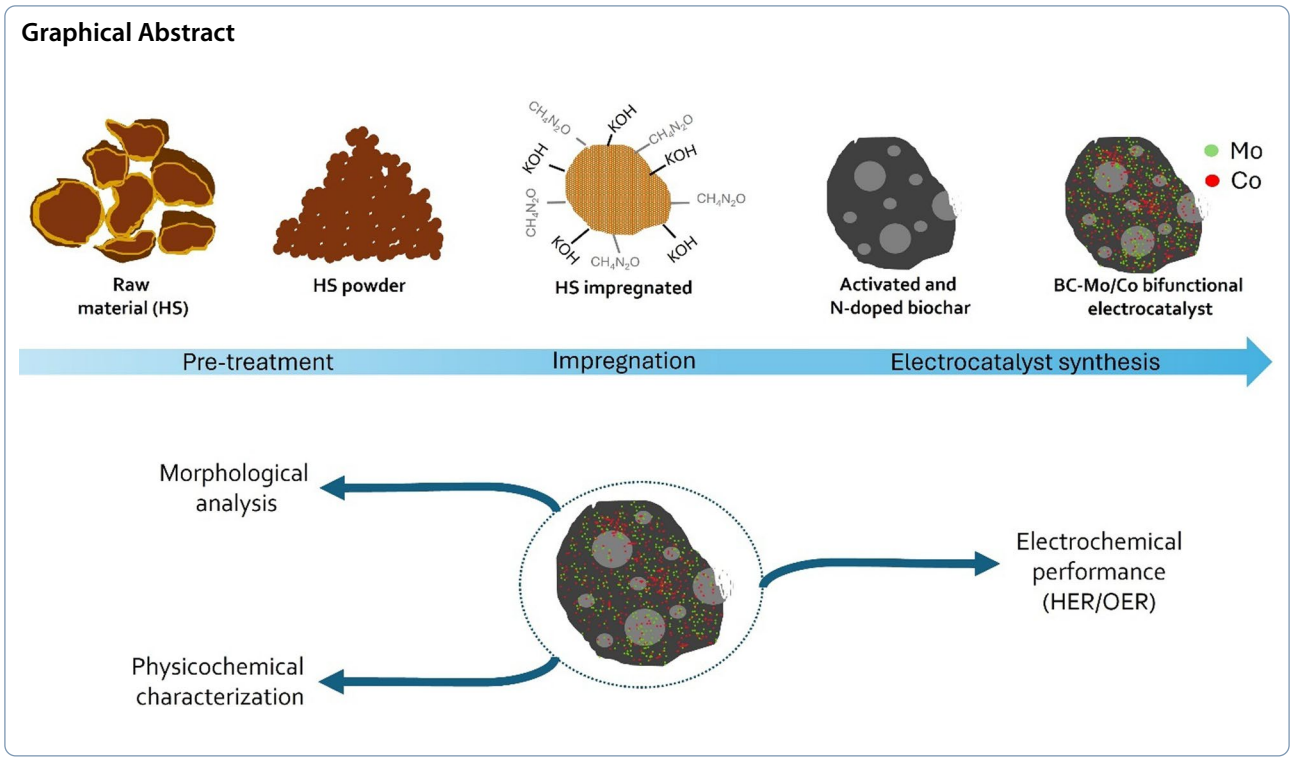

1 Introduction

Global economic, growth historically driven by fossil fuels, has come at the cost of significant environmental impacts, including heightened emissions of CO_2, NO_x, particulate matter, and SO_x (Karmaker et al. 2020; Kober et al. 2020). The risk of a 1.5 °C increase in the average global temperature by 2030, set by the Paris Agreement as a point of no return, is high due to the irreversible consequences that would affect different ecosystems worldwide. To address this challenge, the focus has shifted to the development of renewable energy carriers with minimal environmental impact that can drive sustainable economic growth (Velazquez Abad and Dodds 2020).

In this sense, the research and interest of several countries in green hydrogen through electrolysis production has increased, since it has a calorific value of 122 MJ kg^{-1}, energy equivalent to 2.75 kg of gasoline, so its use represents a better energy efficiency (Sarangi and Nanda 2020). Additionally, the production and use of H_2 will have a positive impact on sustainable development, as it is a zero-carbon energy carrier and a reliable alternative for the development of low-carbon transport systems, industrial decarbonization, and heat supply (Velazquez Abad and Dodds 2020).

Electrolysis involves 2 main reactions, the hydrogen evolution reaction (HER) and the oxygen evolution reaction (OER). HER is a reductive reaction that produces H_2 at a theoretical potential of 0 V vs. standard hydrogen electrode (SHE), while in OER, the oxidative reaction to produce O_2 is obtained at a theoretical potential of 1.23 V (Tüysüz 2023). The relationship between HER and OER is intrinsic, so the overpotential (η) must be minimized to develop an efficient electrolysis reaction. One option is noble metal-based electrocatalysts, such as Pt, Pd ($\eta < 0.1$ V for HER) and Ru, Ir ($\eta < 0.3$ V for OER); however, a limitation to their massive use in the production of green H_2 is the high cost and scarcity of these materials, with prices exceeding 100,000 US dollars per kilogram.

To extend the scope of this technology, low-cost and high-catalytic performance materials for electrocatalyst synthesis are required to be used as cathode/anode, catalyzing HER and OER. Many non-noble materials have been used to study their catalytic performance in these reactions, such as oxides, metals, carbides, phosphides, nitrides, and hydrides, among others, highlighting Mo and Co (Chang et al. 2022; Cui et al. 2020). Although transition metals exhibit higher overpotentials compared to noble metals, they have a significantly lower market price. Moreover, Mo and Co stand out due to their high catalytic performance and stability across different pH conditions, as their Gibbs free energy for hydrogen and oxygen adsorption is close to the optimal value, a characteristic typical of metals with 3d orbitals (Bhunia et al. 2023; Li et al. 2023). However, most of these materials require a high surface

area, porous, and electron transfer support, which allows synthesizing electrocatalysts with a high and uniform distribution of active sites, offering hierarchical channels for the diffusion of reagents/products, such as graphene structures and carbon nanotubes (CNT), which have a market value of more than US$ 5000 per kilogram, and with a complex synthesis (Liu et al. 2021; Pingkuo and Yi 2019). Thus, there is a need to explore innovative, cost-effective, and sustainable electrocatalysts.

A promising alternative is activated biochar derived from waste, which is produced through pyrolysis. This thermochemical treatment is conducted in an inert atmosphere, transforming the raw material into high-value products such as bio-oil, syngas, and biochar (Fahmy et al. 2020). This carbonaceous material exhibits high surface area, excellent chemical stability, and superior adsorption capacity, with applications in soil remediation (Nguyen et al. 2023), fertilizers (Mashamaite et al. 2024), pollutant treatment (Jagadeesh and Sundaram 2023), and as a support catalyst (Pereira Lopes and Astruc 2021). Activated biochar, produced at T > 700 °C, provides better graphitization, larger surface area, and a more ordered carbon structural network, which improves electronic conductivity, active site distribution, and mass diffusion (Singh et al. 2021). Additionally, biochar-doped, such as nitrogen (N), either by in situ doping or impregnation, enhances its hybridization and electronic transfer properties, thereby improving catalytic performance (Deng et al. 2021). Research on the design of biochar-supported electrocatalysts has increased in recent years, exploring the synthesis with Mo and Co precursors. However, it is necessary to study the electrocatalytic performance of Mo/Co bimetallic carbides and their distribution in hierarchically porous structures for HER and OER (Guo et al. 2024; Nguyen et al. 2024). Moreover, several studies suggest that to enhance the scalability of electrocatalysts, bifunctional structures capable of catalyzing both HER and OER should be designed (Park et al. 2022; Xu et al. 2025).

For this purpose, an abundant agro-industrial waste is the shell of European hazelnut (*Corylus avellana* L.), which is one of the most consumed nuts in the world, with Chile being the largest producer in the Southern hemisphere (20,000 tons per year) (Duran et al. 2022; Król and Gantner 2020). Hazelnut shells constitute 50% of the total weight of the fruit and have a high carbon and lignin content, offering a great potential for successful pyrolysis at elevated temperatures.

Therefore, in this work we report a simple methodology for the synthesis of Mo/Co electrocatalysts supported on activated-doped-biochar derived from hazelnut shells, with excellent physicochemical properties, allowing their bifunctional application in HER/OER electrocatalysis at low overpotentials and high stability, offering an interesting alternative that links waste valorization and the development of green hydrogen as a renewable energy source.

2 Materials and methods

2.1 Electrocatalyst synthesis

The hazelnut shells (HS) (*Corylus avellana* L.) were obtained from the agroindustry in Chile. First, HS were washed with abundant water and dried at 80 °C for 8 h. Subsequently, HS were ground in a blade mill, where the particle size was reduced to <1 mm, and additionally, it was ground in a centrifugal mill (Retsch ZM-200) at 8000 rpm, resulting in HS < 120 µm. 20 g of HS was impregnated with 40 g of KOH and 20 g of CH_4N_2O in deionized water (1 L) with stirring at 800 rpm for 6 h at room temperature. It was centrifuged (Eppendorf 5804) in 250 mL bottles at 4000 rpm for 3 min. Finally, the supernatant was removed, and the paste was dried at 105 °C overnight. BC was produced by pyrolysis at 885 °C for 1.5 h under an N_2 atmosphere (120 mL min^{-1}) and a heating rate of 40 °C min^{-1}. Subsequently, BC was crushed in an agate mortar, washed with deionized water and 1 N HCl until neutralized, dried at 105 °C overnight, and sieved at 50 µm. For the BC-Mo/Co synthesis, 0.1 g BC, 0.19 g $Co(NO_3)_2{\cdot}6H_2O$, and 0.07 g $(NH_4)_6Mo_7O_{24}{\cdot}6H_2O$ were mixed in 5 mL ethanol, which was sonicated for 1 h and evaporated at 80 °C under magnetic stirring. Finally, it was dried overnight at 105 °C and pyrolyzed at 800 °C for 2 h in a N_2 atmosphere at a heating rate of 10 °C min^{-1} (Fig. 1). The samples analyzed were BC (biochar activated-doped), BC-Mo (BC-molybdenum), BC-Co (BC-cobalt), and BC-Mo/Co (molybdenum and cobalt supported on BC). Figure S1, Supporting Information, presents the pyrolysis system constructed.

2.2 Physicochemical characterization

Hazelnut shell samples were analyzed by FTIR (Agilent Cary 630), XRF (S4 T-Star, Bruker), elemental (EA 3000, Eurovector), and TGA (STA-6000, Perkin Elmer), to study the characteristics of the raw material. The porosimetry analyses (Nova 1000e, Quantachrome) were performed by N_2 adsorption isotherm (degassing at 160 °C for 16 h), where BET, BJH, and NLDFT were determined. SEM–EDS (SU 3500, Hitachi), and FESEM (INSPECT F50, FEI) did the morphology of the electrocatalyst. Raman spectroscopy was conducted using a Jovin Yvon LabRaman HR800 in the 1100–2000 cm^{-1} range employing a 532 nm laser and calibrated using a silicon reference. X-ray diffraction (XRD) analysis was performed using a PANalytical X'Pert PRO MPD Alpha1 powder diffractometer with Fe-filtered Co Kα

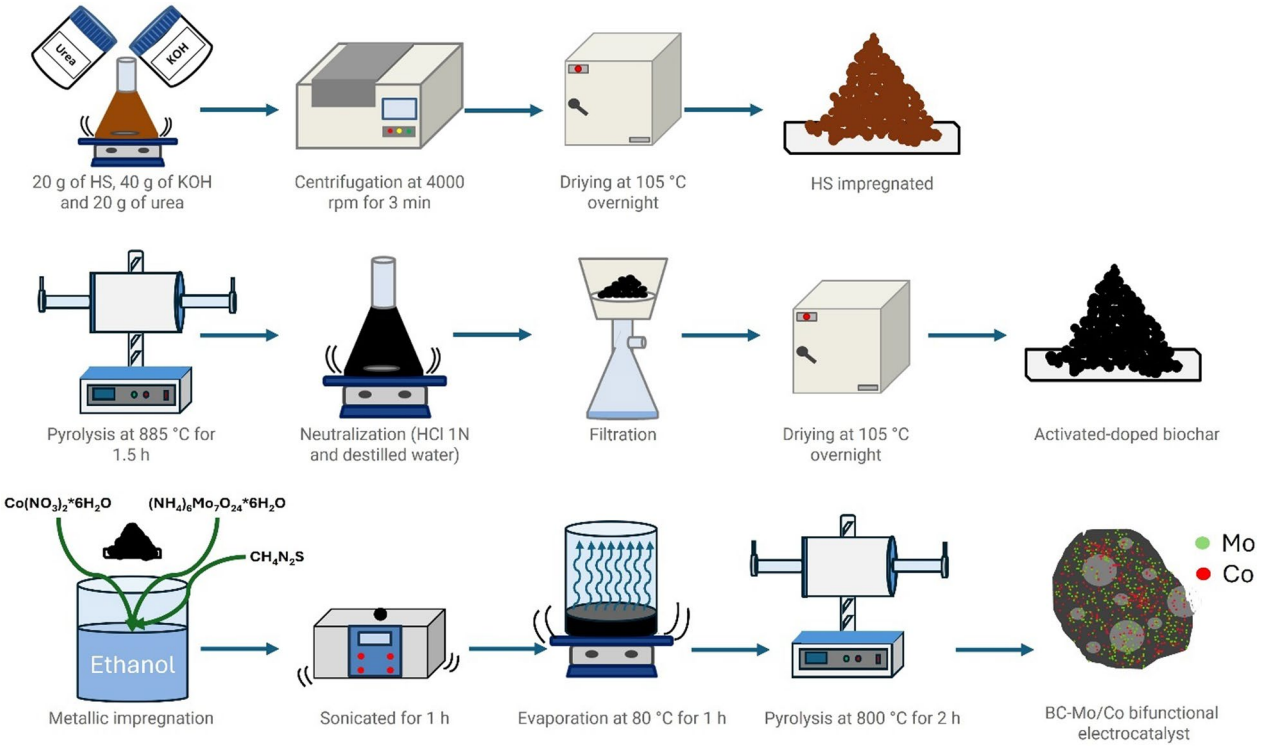

Fig. 1 Schematic representation of the synthesis of electrocatalysts

radiation (λ = 1.789 Å) working at 45 kV to 40 mA in a Bragg Brentano configuration. X-ray photoelectron spectroscopy (XPS) spectra were recorded using an ESFOSCAN, an equipment based on the PHI 5000 VersaProbe 4 from Physical Electronics (ULVAC-PHI), with monochromatized Al Kα radiation (1486.6 eV).

2.3 Electrochemical characterization

Electrochemical measurements were performed on a VSP potentiostat (Biologic), with an RHE reference electrode (Gaskatel, Germany), Pt counter electrode (1 mm diameter), and glassy carbon working electrode (3 mm diameter). Measurements were performed in triplicate. The electrolyte solutions were purged with gaseous N_2 for 15 min. To characterize the biochar, 6 mg of sample was taken and dispersed in a mixture of 800 µL of ultrapure water, 200 µL of ethanol, and 100 µL of 5 wt% Nafion, and sonicated for 30 min. The load used in the glassy carbon electrode was 5 µL, after drying at 60 °C for 15 min.

Linear sweep voltammetry (LSV) was used to determine the overpotential in an alkaline medium (1 M KOH). Scan rates were 2 mV s^{-1} for HER and 5 mV s^{-1} for OER. Electrode potentials were corrected by software with a 95% ohmic drop compensation (IR). The Tafel slope was obtained from the linear Butler–Volmer equation (1). The electrochemical surface area (ECSA) was obtained by (2) (Karmakar and Kundu 2023), where C_s is 40 µF and C_{dl} by half-slope of the linear Δj fit, obtained by cyclic voltammetry between 1.1 and 1.2 V at 20–220 mV s^{-1}. Electrochemical impedance spectroscopy (EIS) was made between 1 MHz and 1 Hz with 10 mV amplitude at −0.4 V (HER) and 1.7 V (OER). Turnover frequency (TOF) was estimated using (3) (Xiao et al. 2023), considering the metal charge of the electrocatalyst as active sites.

$$\eta = \frac{2.303RT}{\alpha nF}\log\left(j_0\right) + \frac{2.303RT}{\alpha nF}\log\left(j\right) \quad (1)$$

where α: transfer coefficient, n: number of electrons transferred, F: Faraday constant, j_0: exchange current density, j: total current, η: overpotential.

$$ECSA = \frac{C_{dl}}{C_s} \quad (2)$$

where ECSA: electrochemical surface area, C_{dl}: capacitance double layer, C_s: specific capacitance.

$$TOF = \frac{jA}{eFn} \quad (3)$$

where j: density current, A: surface glassy carbon electrode, e: number of electrons transferred (2 for HER and 4 for OER), n: number of active sites.

3 Results and discussion

3.1 HS characterization

Several preliminary analyses were performed to characterize the nature of HS. The elemental composition of HS (Table S1, Supporting Information) showed a high carbon content (<53%). The thermochemical degradation of HS was studied by proximal TGA (Fig. S2, Supporting Information), yielding 21.7% fixed carbon and 71.8% volatile solids, with a Derivate Thermogravimetric (DTG) of 371 °C, corresponding mainly to cellulose and hemicellulose degradation (Ceylan and Topçu 2014). The ash content corresponded to 0.347%, characterized by TXRF (Fig. S3, Supporting Information), where small amounts of Mg, Cl, and K were detected. In the FTIR spectrum (Fig. S4, Supporting Information), a decrease in transmittance was observed between 3600 and 3200 cm^{-1}, characteristic of the O–H bond, indicating the presence of alcohol or phenol groups, and N–H bond, corresponding to amine groups (Xu et al. 2017). 2900–2800 cm^{-1} asymmetric C–H bonds (CH_2 and CH_3) were detected for methyl and methylene, related to lipids (Dogan et al. 2007). The C=O bond was detected at 1746 cm^{-1} and the C=C bond at 1630 cm^{-1} (Şencan et al. 2015). The C–O bond was identified at 1040 cm^{-1}, which is characteristic of alcohols, ethers, and esters groups (Xu et al. 2017). Finally, the curves corresponding to biochar showed the volatilization of radical groups, except for the peaks detected at 2140–2070 cm^{-1} and 1990 cm^{-1}, which can be related to compounds such as CO and CO_2 (Söyler and Ceylan 2021), as well as the presence of C–N, C≡C, C=C=N, and N=N (Almazán-Sánchez et al. 2015; Deng et al. 2021; Şencan et al. 2015). The BC-Mo, BC-Co, and BC-Mo/Co samples showed the same peaks as biochar, but with higher intensities, characteristic of pyrolysis at high temperatures and graphitization of the structure.

3.2 Morphological characterization

The morphological changes in the biochar support and its subsequent decoration were analyzed by SEM (Fig. 2). The pyrolysis of HS at 885 °C for 1.5 h without KOH (Fig. 2a) produced a biochar with low porosity and rough surface, where these characteristics

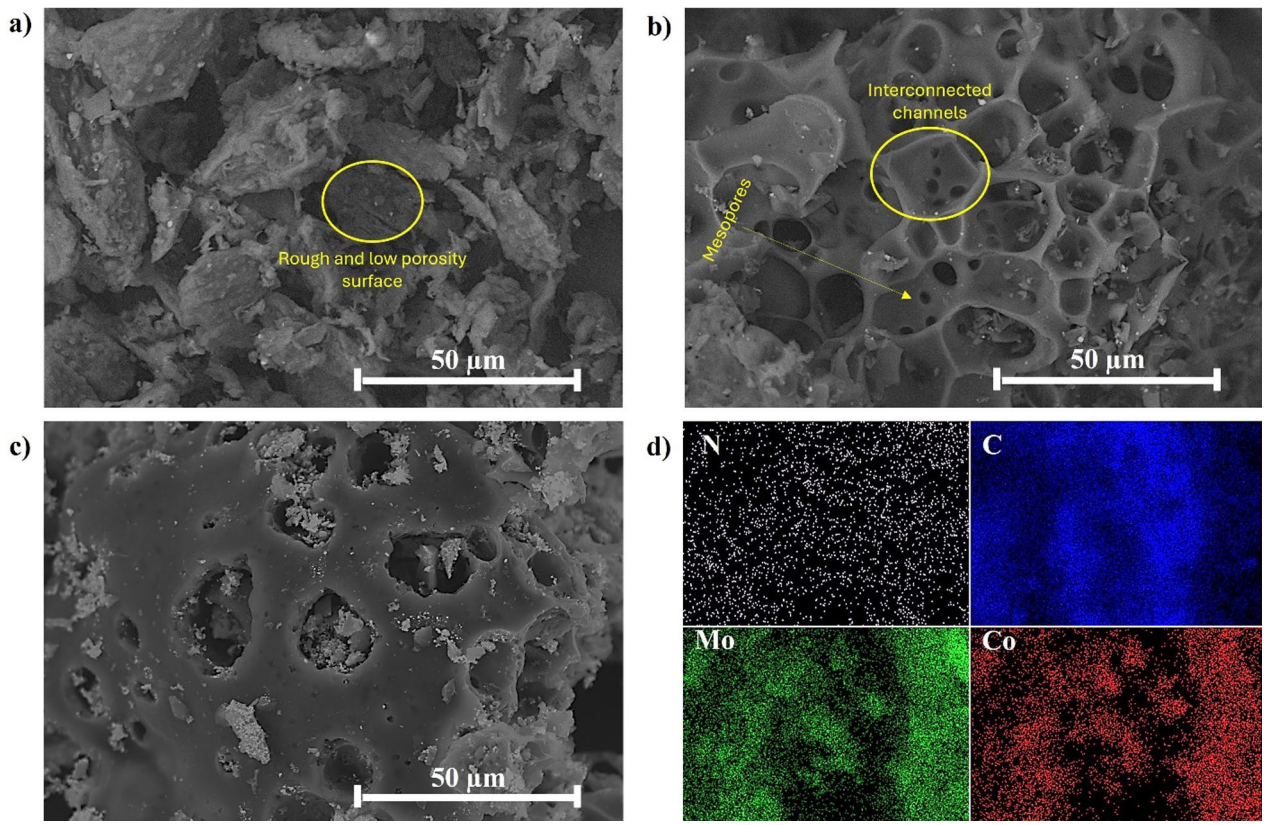

Fig. 2 SEM images of **a** non-activated biochar pyrolyzed at 800 °C for 2 h, **b** activated biochar pyrolyzed at 800 °C for 2 h, **c** Mo/Co supported on biochar, and **d** mapping showing the elemental distribution (carbon, cobalt, and molybdenum)

were exclusively attributed to the thermal degradation of structural compounds (cellulose, hemicellulose, and lignin) and the volatilization of functional groups present in the raw material.(Sakhiya et al. 2020). On the other hand, activated-doped biochar (Fig. 2b) presented a highly interconnected pores formation, which provides a larger surface area and a well-developed pore network, enhancing mass transfer through increased exposure of catalytic sites, thus improving the adsorption–desorption kinetics of hydrogen and oxygen during HER and OER (Zhang et al. 2023). Figure 2c shows BC-Mo/Co, where the presence of metals is observed on the external surface of the support and inside the developed macropores, allowing for greater exposure of active sites, primarily composed of C, N, Mo, and Co (Fig. 2d). FESEM was used to analyze the BC-Mo/Co morphology in more detail (Fig. 3a), where the formation of fine irregularities on the biochar surface was observed (Fig. 3b), forming shallow pores and allowing greater accessibility of the supported active sites and the reactions involved. In addition, a catalyst matrix growth was evidenced (Fig. 3c, d), with reliefs that increase the exposure of active sites. The incorporation of Mo and Co into the biochar support allows for partial occupation of the pores created through KOH activation. This distribution enhances the interaction between Mo/Co and the C/N structure, facilitating charge transfer and improving catalytic performance in HER and OER, as evidenced by the reduction in overpotential in the electrochemical characterization presented in this work.

3.3 Physicochemical properties

The surface area and pore structure characteristics were obtained from porosimetry analysis. Figure 4a presents the N_2 adsorption–desorption isotherm of activated biochar, where this structure exhibited a high surface area (1102 $m^2\ g^{-1}$). This isotherm corresponds to type-I according to the IUPAC nomenclature, suggesting the formation of interconnected pores with a large number of micropores, which were filling to low pressures (<0.15 P/P_0) because of high adsorbent–adsorbate interaction (Bardestani et al. 2019). The surface areas obtained for BC-Mo, BC-Co, and BC-Mo/Co were 222.5, 234.3, and 321.9 $m^2\ g^{-1}$, suggesting a high use of the surface area offered by the biochar matrix.

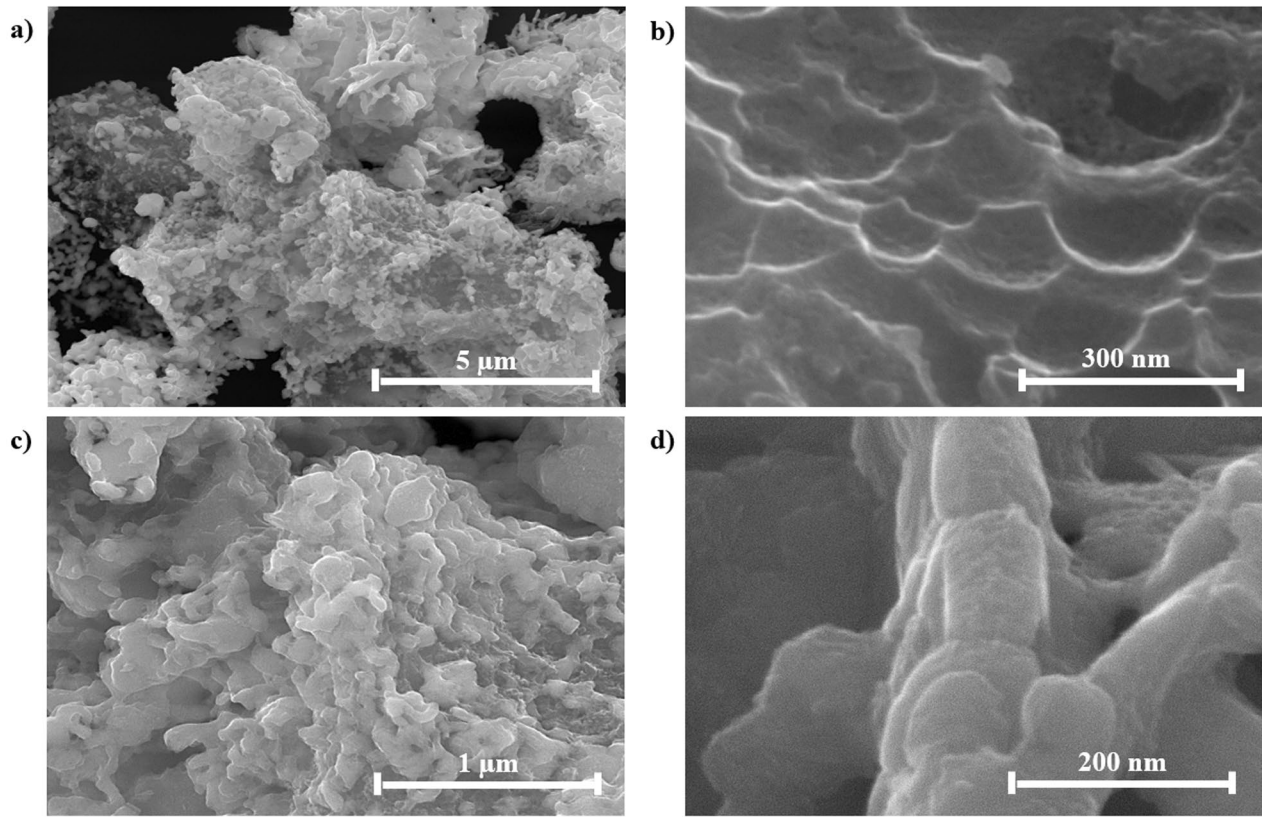

Fig. 3 FESEM of the BC-Mo/Co electrocatalyst at different resolution scales (**a**–**d**)

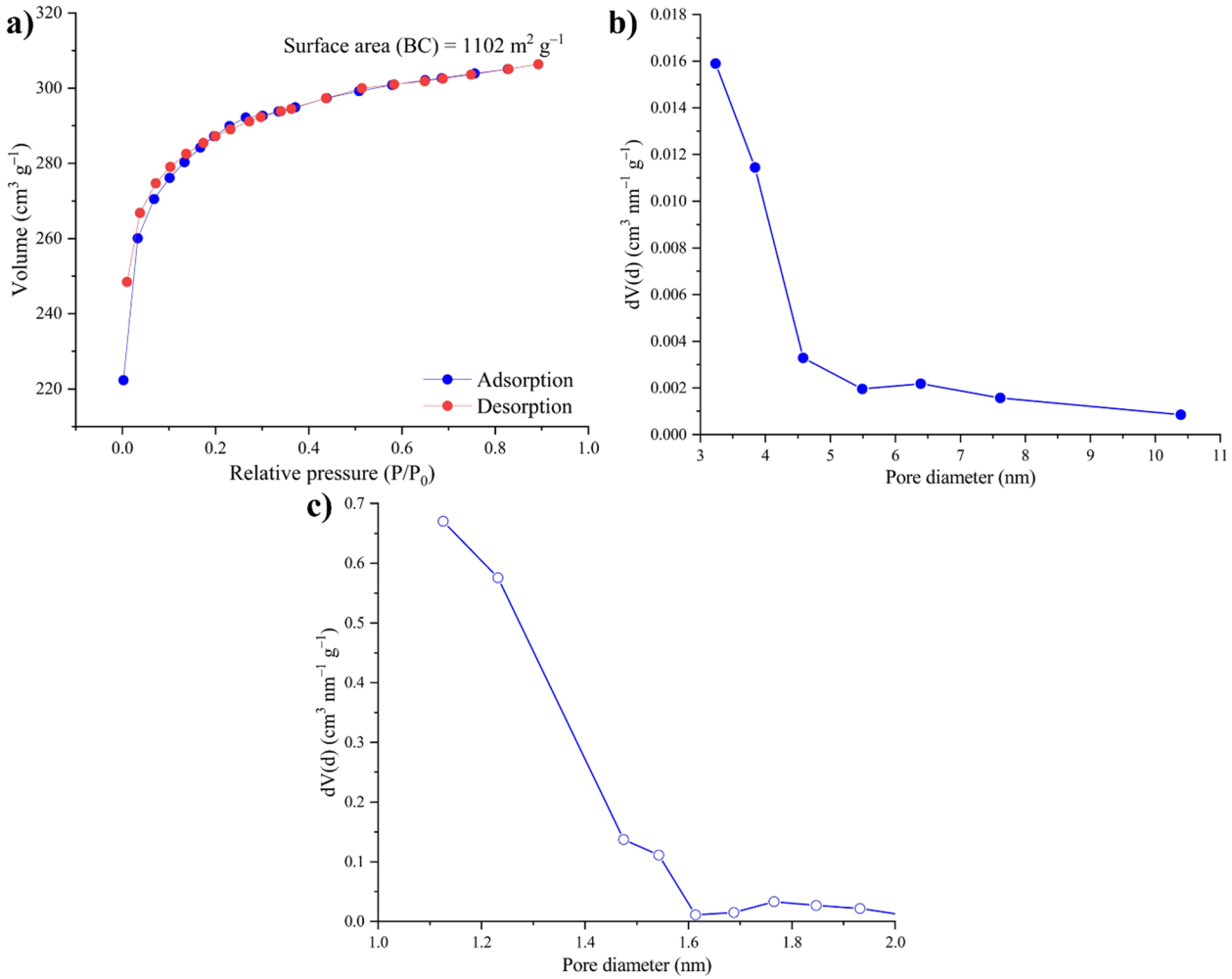

Fig. 4 Porosimetry analysis of biochar sample pyrolyzed at 800 °C: **a** N_2 isotherm and surface area by BET method, **b** size pores distribution between BJH method for mesopores and **c** DFT method for micropores

The KOH-activation is widely used in biochar production due to its strong affinity with biomass and thermodynamic favorability at high temperatures (Dehkhoda et al. 2016). The reaction mechanism is presented below (Tsubota et al. 2021):

$$2KOH \rightarrow K_2O + H_2O \quad (4)$$

$$6KOH + 2C \rightarrow 2K + 3H_2 + 2K_2CO_3 \quad (5)$$

$$K_2CO_3 + 2C \rightarrow 2K + 3CO \quad (6)$$

$$K_2CO_3 \rightarrow K_2O + 2CO_2 \quad (7)$$

$$K_2CO_3 + C \rightarrow K_2O + 2CO \quad (8)$$

$$K_2O + CO_2 \rightarrow K_2CO_3 \quad (9)$$

$$K_2O + C \rightarrow 2K + CO \quad (10)$$

Reactions (4)–(7) and (10) are responsible for pore formation through gas generation, while reactions (5), (8), and (10) involve biomass degradation, resulting in pore formation and corrosion of its walls. From a thermodynamic perspective, a reaction is spontaneous when its $\Delta G_r < 0$, a state achieved by reactions (5) and (9) starting at 800 °C (Tsubota et al. 2021). Since reaction (9) does not involve pore formation but rather a precursor, the reaction that contributes most to pore production is (5), a finding supported by other studies (Dehkhoda et al. 2016; Qu et al. 2021; Zhu et al. 2021). Likewise, the KOH treatment is effective at high temperatures due to the potassium boiling

point (760 °C), which improves its diffusion in the carbon structure and increases the surface area on the inner walls of the pores. Figure 4b and c shows the pore size distributions by BJH and DFT for BC (activated-biochar at 885 °C for 1.5 h), respectively. By the mesopore distribution BJH, an average volume and diameter of 0.029 cm^3 g^{-1} and 3.232 nm were determined, while the micropore distribution by DFT presented 0.423 cm^3 g^{-1} and 1.126 nm, evidencing the configuration of a hierarchical porous structure.

Raman spectroscopy of the electrocatalysts is presented in Fig. 5. As is characteristic of biochar samples, the carbon identification is represented by the D-band (1350 cm^{-1}) and G-band (1590 cm^{-1}) (Xu et al. 2020). The D-band corresponds to the amorphous structure of carbon (sp^3), while the G-band is mainly attributed to the graphite crystallite, where the carbon is arranged in graphitic layers through sp^2 hybridized bonds (Deng et al. 2021). The I_D/I_G ratio indicates the degree of structural defect level in the sample. An $I_D/I_G < 1$ is typical of materials with high structural order, whereas $I_D/I_G > 1$ corresponds to materials composed mainly of amorphous carbon (García-Rocha et al. 2023). In this case, BC had an $I_D/I_G = 1.08$, so the biochar structure presents graphitic sites, which are beneficial for electrocatalysis. A relevant factor for this indicator is the pyrolysis temperature, as it is directly proportional to the carbon ordering through the graphite layers superposition for π bonds (Chen et al. 2023), which improves the electrical conductivity at pyrolysis temperatures above 600 °C (Gabhi et al. 2020). The activated-doped biochar improved its graphitization due to the coupling of N atoms in the graphite layer, allowing its growth, which is enhanced for K diffusion in the microporous structure, increasing the electron vacancy in the d orbitals (Kiciński and Dyjak 2020). The addition of the metal in biochar increased the defect proportions on the surface, obtaining an $I_D/I_G < 1$, showing a higher graphitization of the carbon in the electrocatalyst. Similar examples are observed with the addition of iron in carbonaceous structures, where some catalysts promote graphitization of the carbonaceous matrix, such as iron (Romero Millán et al. 2023) and calcium (Béguerie et al. 2022), enhancing electron transfer.

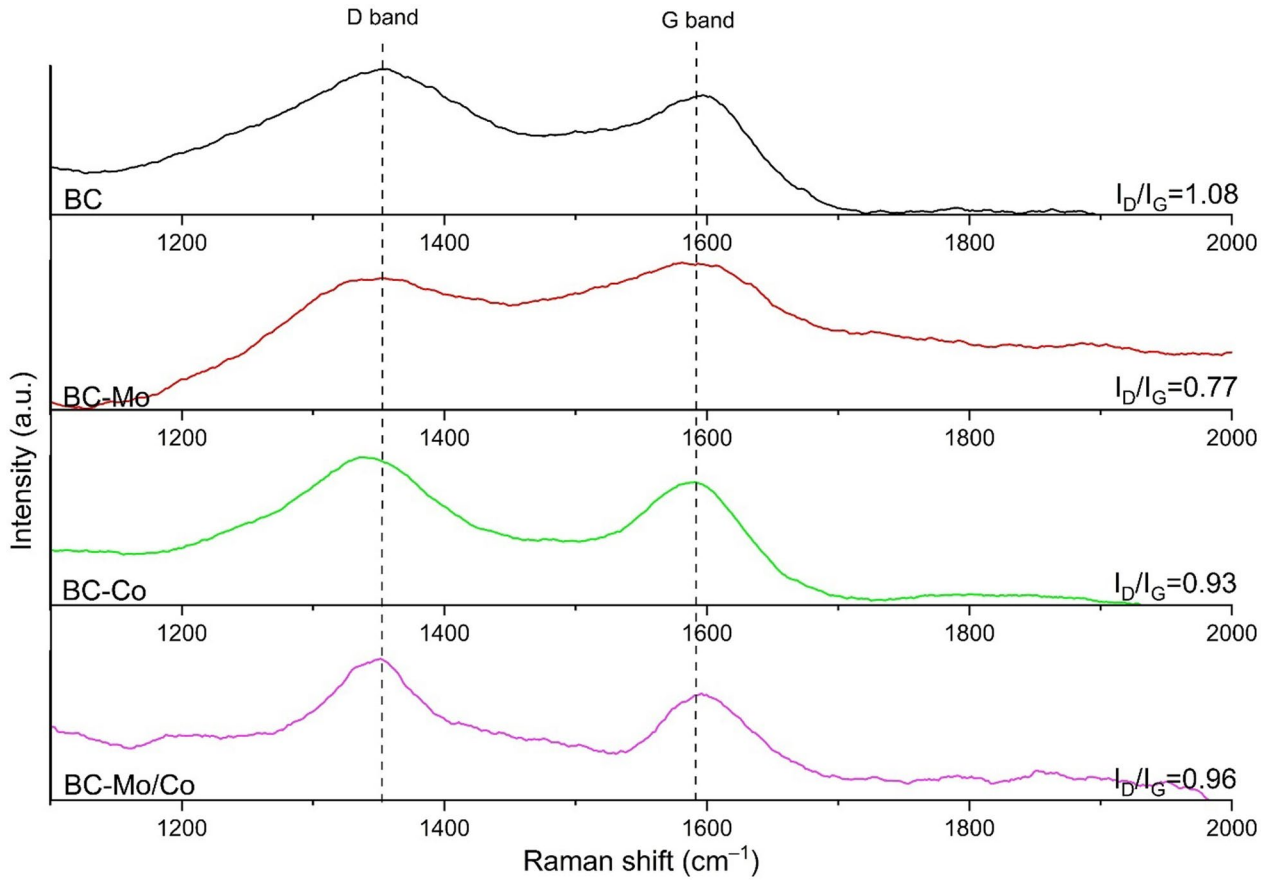

Fig. 5 Raman spectra of synthesized electrocatalysts

XRD patterns (Fig. S5, Supporting Information) show the amorphous and graphite carbon at 22° and 44°, respectively (Guo et al. 2020a, b). Amorphous carbon has a disordered structure and low electron transfer capacity due to its high internal resistance (Mittal et al. 2023), while graphitic carbon (101), detected at 44° (JCPDS 41-1487), is more ordered. However, it should be noted that the amorphous carbon region overlaps with the (002) graphitic carbon at 26°, which is more crystalline than the (101) plane, which is characteristic of graphene structures, obtaining a higher electrocatalytic capacity (Neeli and Ramsurn 2018). Additionally, BC-Mo, BC-Co, and BC-Mo/Co were characterized by XRD to study the crystal structure of the catalyst (Fig. 6). In the case of BC-Mo, a transition oxidize-reduced state was evidenced, with MoO_2 monoclinic (JCPDS 01-078-1070), γ-Mo cubic metallic (JCPDS 01-089-5156), Mo_2C orthorhombic (JCPDS 01-079-0744) and hexagonal (JCPDS 035-0787) structures detected. The BC-Co sample showed a reduction in the crystalline metallic Co (JCPDS 015-0806), mainly due to pyrolysis conditions, which also improved the graphitization of the biochar. This is interesting, as cobalt can be a catalyst for biochar graphitization, forming a carbon ordering at the edges of the cobalt metal (Tian et al. 2022), similar to that occurs in graphitization catalytic by iron on biochar structure (Sagues et al. 2020). In BC-Mo/Co, Co enhanced the carbides synthesis, increasing the density of Mo_2C and formation of $Co_6Mo_6C_2$ (JCPDS 01-080-0339), a carburized Mo-Co phase with good catalytic performance in combination with carbonaceous structures (Yaseen et al. 2022). This compound is formed at 750 °C and maintains its stability up to 850 °C, a phase before Mo_2C and metallic Co (Dong et al. 2023). Metallic Co and $Co_2Mo_3O_8$ (JCPDS 034-0511) were also detected.

The BC-Mo/Co surface was analyzed by XPS (Fig. 7a), where signals of C, O, Mo, Co, and N were detected. Between 392 and 402 eV, the deconvolution of N 1s and Mo 3p was shown, where a high presence of pyridinic-N and the formation of N-Mo bonds were observed, which have an important catalytic activity (Fig. 7b). In the case of Mo (Fig. 7c), three important signals were observed between 228 and 238 eV (Mo 3d), where the peaks at 228.6 and 231.8 eV correspond to Mo^{2+} (β-Mo_2C), while the peaks at 229.5 eV and 233.0 eV are Mo^{3+}, characteristic of Mo–N bonds. The remaining contributions

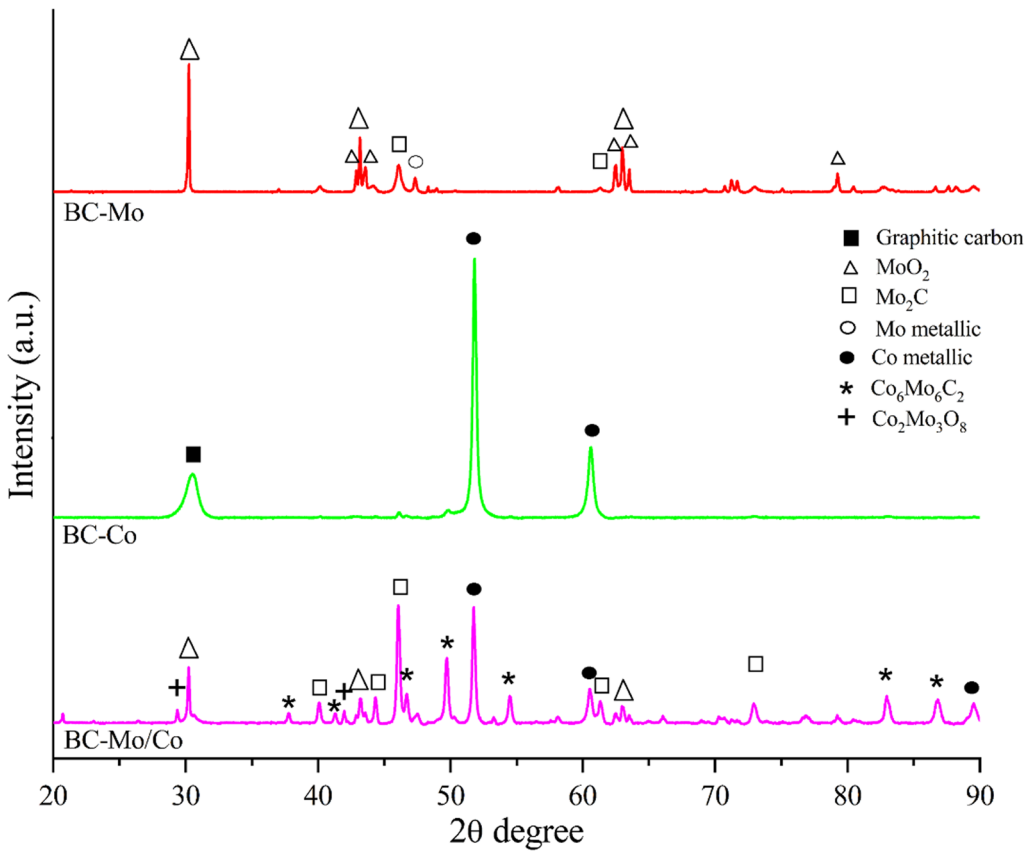

Fig. 6 XRD diffractograms of Mo, Co, and Mo/Co electrocatalysts supported on biochar

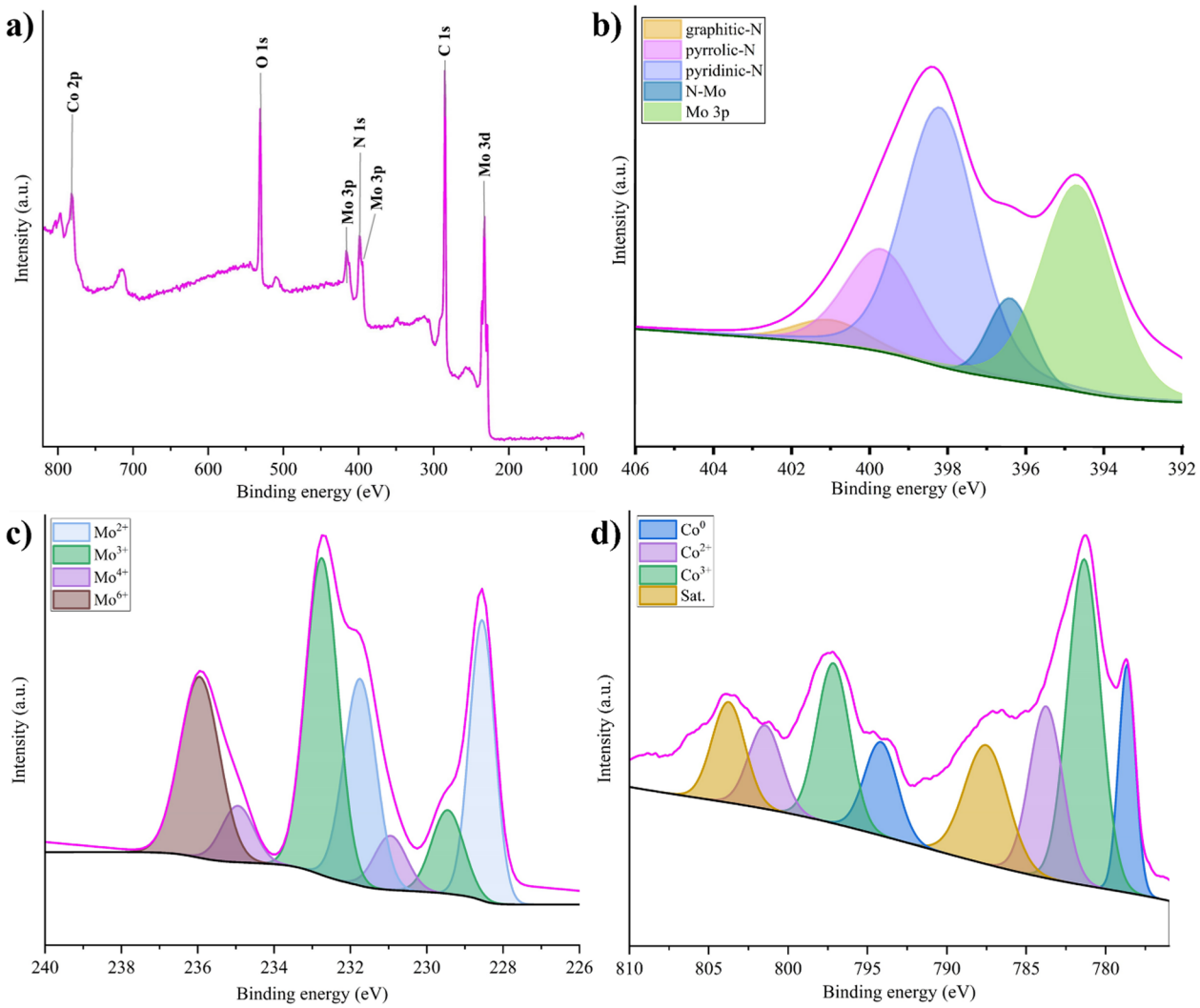

Fig. 7 General XPS spectra of **a** BC-Mo/Co, and high resolution for **b** N 1s, **c** Mo 3d, and **d** Co 2p

(230.5 eV, 233.8 eV, and 232.6, 235.8 eV) are attributed to Mo^{4+} and Mo^{6+}, characteristic of surface oxidation over time (Guo et al. 2020a, b). Co signals (Fig. 7d) were detected between 778.5 and 793.7 eV, where the deconvolution evidenced the presence of spin-orbits of $2p_{1/2}$ and $2p_{3/2}$, corresponding to Co^{2+} and Co^{3+} (782.5/799.4 eV and 780.3–796.2 eV, respectively) and Co^0 (778.5 and 793.7 eV) (Ge et al. 2022; Wang et al. 2017). Between 283 and 286 eV, C 1s was detected (Fig. S6, Supporting Information), whose contributions were associated with C-Mo (283.7 eV), C–C/C/C=C (284.7 eV), and C–N/C=N (285.8 eV) (Guo et al. 2020a, b) bonds that were also determined by FTIR (Fig. S4, Supporting Information). The analysis of these spectra confirms the graphitization trend of the biochar, the nitrogen doping, and the presence of Mo/Co with high catalytic capacity.

3.4 Electrocatalytic activity

3.4.1 HER performance

First, the performance of the electrocatalyst was determined using linear sweep voltammetry (LSV) to estimate the overpotential needed for the hydrogen evolution reaction (HER), setting η_{10} as the overpotential to reach a current density of 10 mA cm^{-2}, since this is the most used to compare the performance of different electrocatalysts (Zhu et al. 2020). This study observes a clear overpotential trend due to the biochar decoration. Thus, BC presented an overpotential of 0.505 V, which was decreased with the addition of metals, such as BC-Mo (0.428 V) and BC-Co (0.345 V), respectively, with the lowest overpotential obtained in BC-Mo/Co with 0.257 V for HER (Fig. 8a).

For the kinetic study, Tafel curves were obtained for each sample. Among the parameters of these

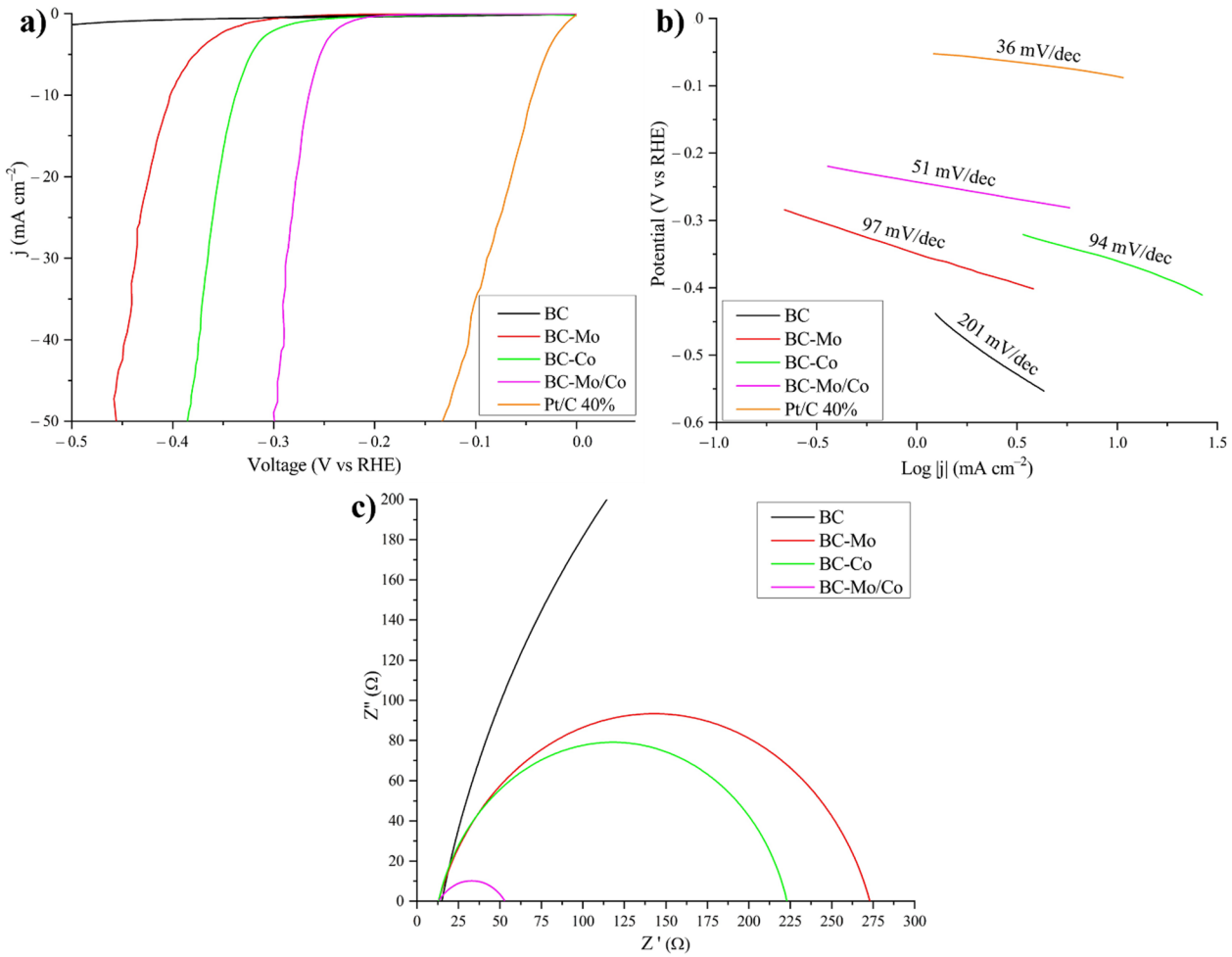

Fig. 8 HER performance of electrocatalysts: **a** linear sweep voltammetry (1 M KOH at 2 mV s^{-1}), **b** Tafel slope, and **c** Nyquist plots (at 0.4 V)

curves, the Tafel slope is the most important, as it is used to understand the catalytic performance of the electrocatalyst and the reaction mechanism adopted (Anantharaj and Noda 2022). In HER, electrochemical hydrogen adsorption is governed by the Volmer reaction, while hydrogen desorption can be electrochemical (Heyrovsky reaction) or chemical (Tafel reaction) (Zhu et al. 2020). These reactions have definite Tafel slopes, being 120, 40, and 30 mV dec^{-1} for the Volmer, Heyrovsky, and Tafel reactions, which is very useful for elucidating the determining step of the reaction (Li et al. 2020). In this study, the synthesized electrocatalysts presented a trend in decreasing the Tafel slope (Fig. 8b), with BC-Mo/Co presenting the lowest value (51 mV dec^{-1}) and relatively close to that of 40 wt% Pt/C (36 mV dec^{-1}).

Electrochemical impedance spectroscopy (EIS) has been employed to further study the electrode–electrolyte interface. This tool helps to determine the charge resistance and mass transfer, directly impacting the kinetics of the reaction (Lazanas and Prodromidis 2023). Figure 8c presents the Nyquist plots for HER, measured at −0.4 V potential. The equivalent circuit is presented in Fig. S7, Supporting Information. All the samples presented an R_s of 13 Ω, considering the resistance of the solution, the distance between the reference-working electrode, and connections, among others. The R_{ct} resistances were the ones that presented the most remarkable differences, where BC had 2050 Ω, BC-Mo 260 Ω, BC-Co 213 Ω, and BC-Mo/Co 40 Ω. R_{ct} corresponds to the resistance to charge transfer at the interface between electrocatalyst-electrolyte. The low R_{ct} of BC-Mo/Co suggests a lower charge transfer resistance, which is related to a higher exposure of active sites in a porous structure, which improves the electrocatalytic effectiveness compared to the other samples (Nazari and Ghaemmaghami 2023).

In electrocatalysis, the turnover frequency (TOF) is an intrinsic indicator of the catalytic activity through theoretical production (H_2 or O_2) per time unit, considering the availability of active sites in the electrocatalyst (Anantharaj et al. 2021). In HER (Fig. S8a, Supporting Information), BC-Mo/Co presented the highest TOF (0.12 s^{-1}), unlike BC-Mo (0.012 s^{-1}) and BC-Co (0.079 s^{-1}). The stability of the BC-Mo/Co electrocatalyst was measured by chronoamperometry at −0.257 V, which is presented in Fig. S8b, Supporting Information, presented excellent stability towards HER in an alkaline medium, with a current drop of about 10% after 25 h of operation, which could be improved by future scaling up of the process.

3.4.2 OER performance

For OER, LSV (Fig. 9a) presents the overpotentials (η_{10}) of BC (0.907 V), BC-Mo (0.471 V), BC-Co (0.446 V), and BC-Mo/Co (0.371 V). As in HER, biochar decoration with Mo/Co had a synergistic effect in reducing the overpotential, suggesting a further availability of active sites dispersed over the high surface area offered by biochar (Yaseen et al. 2022). Figure 9b shows the Tafel slopes for OER, where BC-Mo/Co (59 mV dec^{-1}) was much lower than BC, BC-Mo, and BC-Co, implying better reaction kinetics. The reactions are mainly influenced by hydroxyl adsorption–desorption on active sites, so the heteroatomic decoration of BC-Mo/Co decreases the Tafel slope, improving the OER kinetics (Abdolahi et al. 2021); however, a slope close to 60 mV dec^{-1} suggests that a possible limiting step is the $O–O^{ads}$ formation in active sites availability (Hou et al. 2022).

For EIS (Fig. 9c), the same trend as for the HER was observed in the decreasing of R_{ct}, being the lowest for BC-Co (45 Ω) and BC-Mo/Co (12 Ω). Additionally,

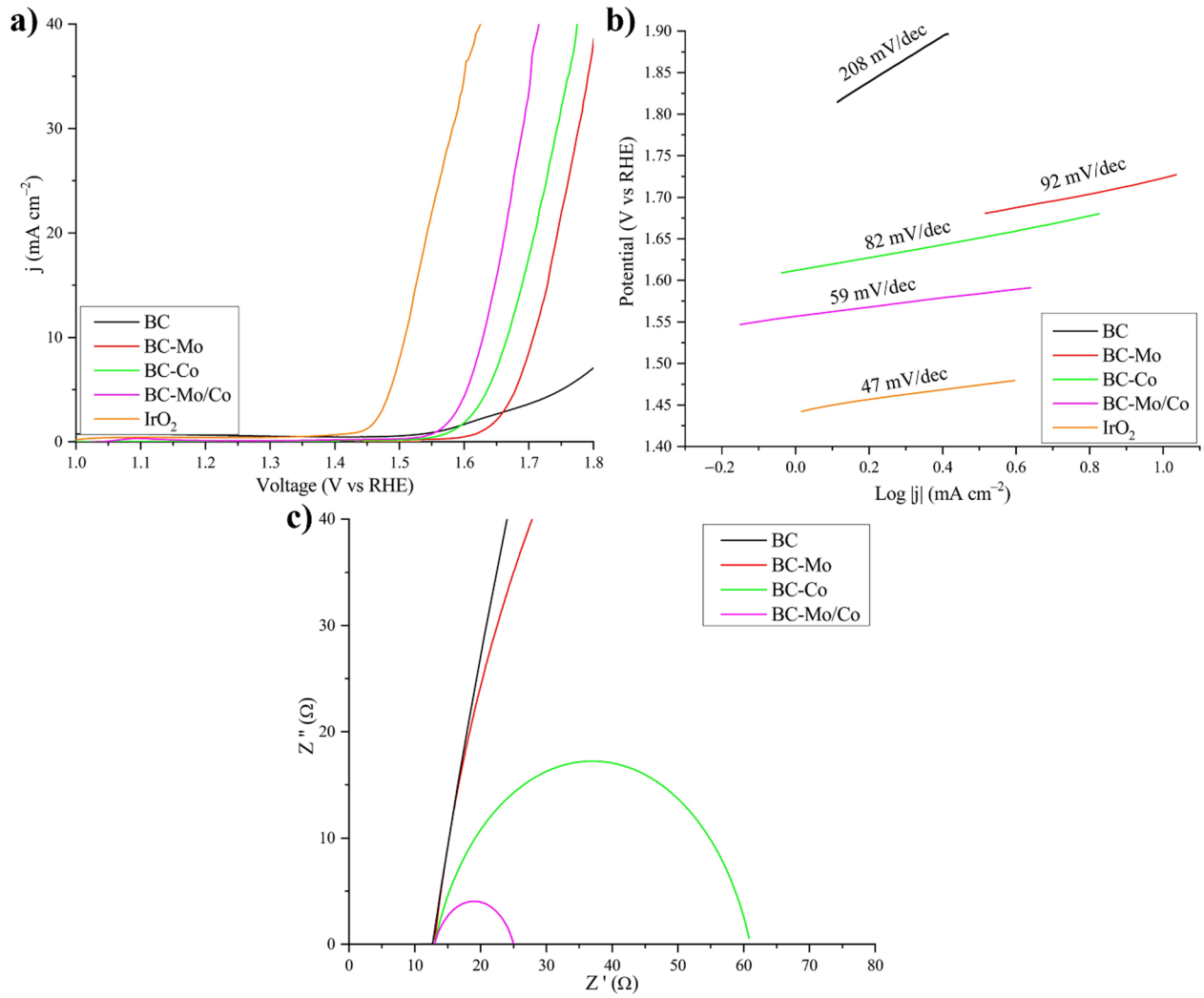

Fig. 9 OER performance of electrocatalysts: **a** linear sweep voltammetry (1 M KOH at 5 mV s^{-1}), **b** Tafel slope, **c** Nyquist plots (at 1.7 V)

the equivalent circuit for HER and OER (Fig. S7, Supporting Information) was obtained, where R_{ct} is connected in parallel with a constant phase element (CPE), which represents the electrical double layer (C_{dl}) at the electrocatalyst-electrolyte interface, participating in the charge transfer process in BC-Mo/C (Lazanas and Prodromidis 2023). In the TOF estimation, the synthesized electrocatalysts showed the same trend as HER (Fig. S9a, Supporting Information), but with lower TOF values compared to HER, with BC-Mo/Co (0.049 s^{-1}) being the most catalytic, followed by BC-Co (0.026 s^{-1}) and BC-Mo (0.019 s^{-1}). This difference can be due to the thermodynamic barrier of OER and the complex desorption of oxygen (Cheng et al. 2018). However, the values obtained in this study are consistent with other noble metal-free electrocatalysts in the form of carbides and phosphides (Guo et al. 2020a, b; Mu et al. 2022). Finally, the BC-Mo/Co stability for OER was determined by chronoamperometry at 1.6 V (Fig. S9b, Supporting Information), where the material showed good stability over 15 h of operation. The current drop may be due to oxidation of the electrocatalyst carbon and excessive bubble formation, which blocks the accessibility to the active sites of the structure. It should be noted that HER/OER are directly related reactions (Fig. 10), with deterministic steps. In HER, the reactions are identified, and as determined by the Tafel slope, H_2 desorption occurs by the Heyrovsky reaction. On the other hand, the OER mechanism is complex and not as agreed as HER, but one of the most studied is the single-site mechanism, where O-O^{ads} formation is a rate determining step (Shinagawa et al. 2015).

The electrochemical surface active (ECSA) through double layer capacitance (C_{dl}) is the most used to determine the catalyst surface that participates in the electrochemical phenomena involved (Anantharaj et al. 2018). For this purpose, cyclic voltammetry was performed in the non-faradaic zone at different scanning speeds, presented in Fig. S10, Supporting Information. The difference between the cathodic and anodic current densities (Δj) was plotted according to the respective sweep speed (Fig. 11), where the half-slope corresponds to C_{dl}. Assuming a standard ECSA of 40 μF cm^{-2} per cm^{-2} (Guo et al. 2020a, b), an ECSA of 1 cm^2 (BC), 9 cm^2 (BC-Mo), 9.4 cm^2 (BC-Co), and 13.8 cm^2 (BC-Mo/Co) was determined, demonstrating that the addition of Mo/Co improved the dispersion and exposure of active sites on the electrocatalyst surface, increasing its catalytic performance and allowing a better mass transfer for the adsorption/desorption in HER/OER (Guo et al. 2020a, b; Liang et al. 2023). The effect of pyrolysis temperature in electrocatalyst synthesis (for 2 h) was also evaluated (Fig. S11, Supporting Information). BC-Mo/Co synthesized at 800 °C obtained the lowest overpotential at η_{10} (0.257 V and 0.371 V for HER/OER, respectively). At 700 °C the

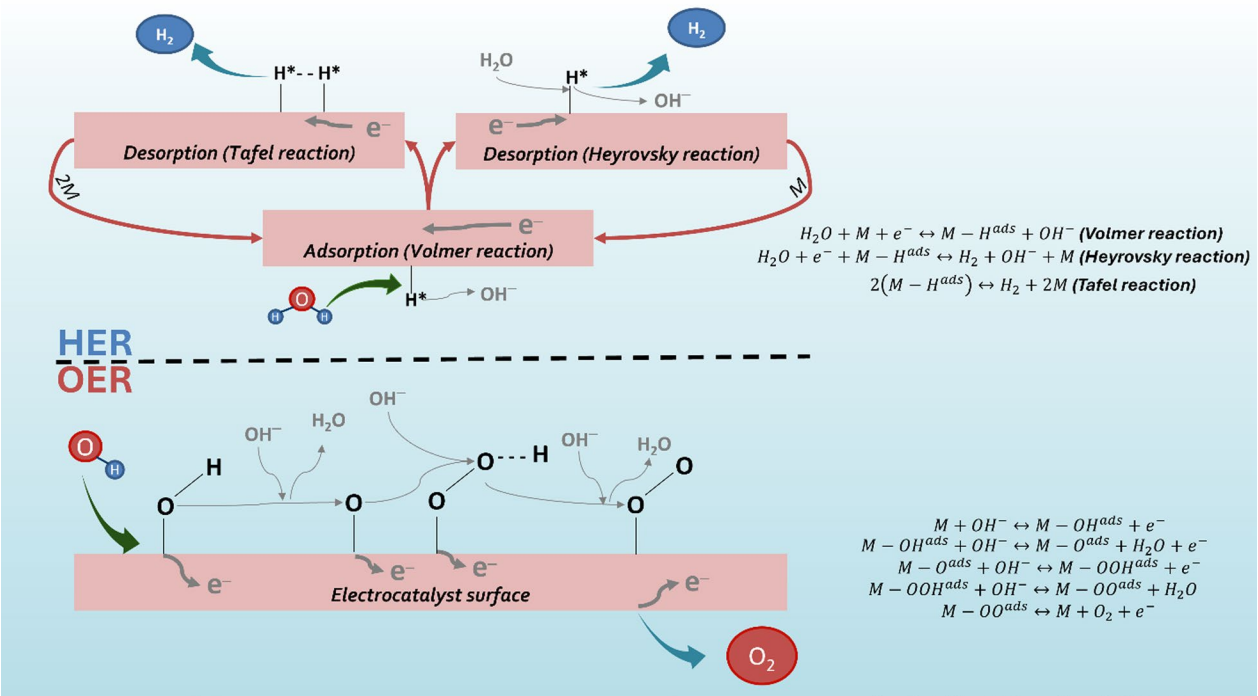

Fig. 10 Reaction mechanism proposed for HER and OER in alkaline medium

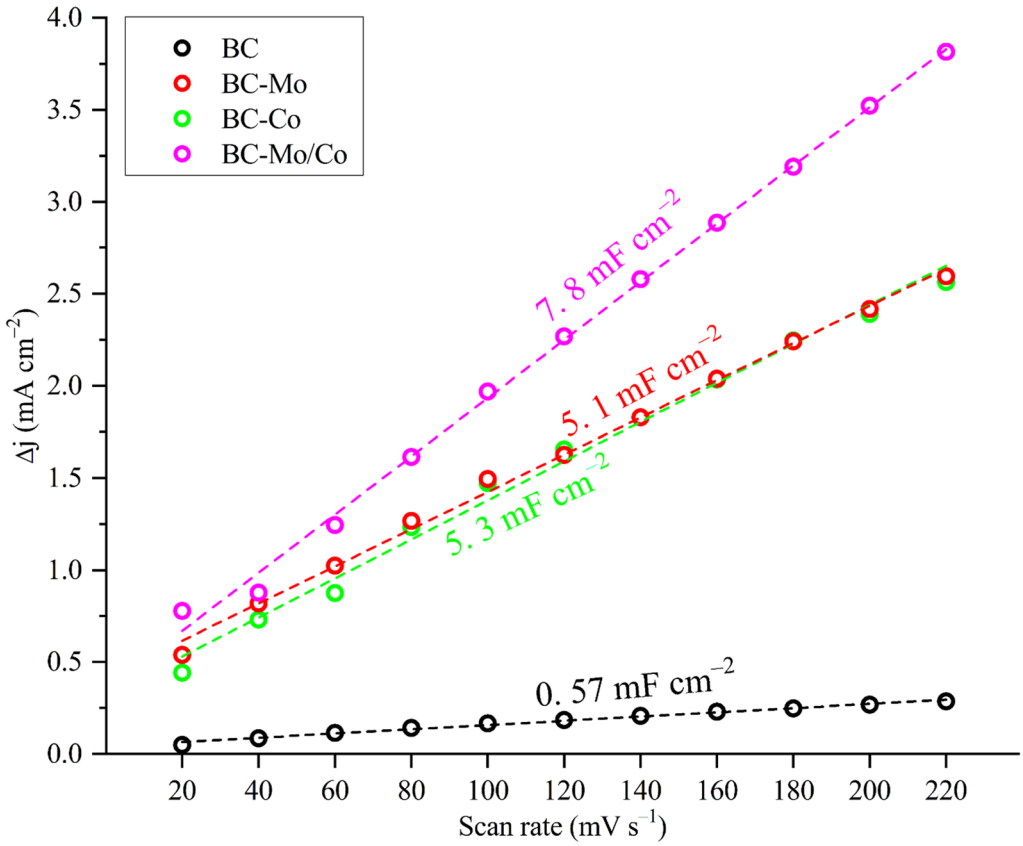

Fig. 11 Linear fitting C_{dl} of catalysts synthesized for ECSA determination

biochar structure does not crystallize sufficiently, resulting in poor electron transfer. On the other hand, temperatures above 800 °C may increase block formation and aggregation of Co and Mo, restricting access to the active sites present in the pores and affecting the mass transfer involved in the reactions (Guo et al. 2020a, b; Han et al. 2019). However, it is observed that the electrocatalyst synthesized at 1000 °C presented a decrease in the OER overpotential, which is because Mo/Co carburization allows these active sites to tend to oxidation, improving the adsorption of OH^- on the surface, a limiting intermediate step in OER catalysis, and thus reducing the overpotential (Jiang et al. 2017).

For comparison, Table 1 presents other relevant research in the design of bifunctional electrocatalysts for HER/OER reactions, free-noble metals, and biochar supports. The present study obtained overpotentials similar to those presented by other authors, evidencing a catalytic improvement of the material. Furthermore, low Tafel slopes were obtained for both reactions, reflecting a high reaction rate once η_{10} is overcome. These results are relevant because this research focused on synthesizing a mixed bifunctional electrocatalyst of Mo_2C and metallic Co, using waste-derived carbonaceous structures, an emerging biochar application. The covalent (Mo_2C) and metallic (Co) bonds present in the electrocatalyst are responsible for its catalytic performance, evidencing a synergistic effect between Mo, C, and Co ($Co_6Mo_6C_2$). The stability of these bonds is observed in their low current drop during operation. These first results are relevant to seek the reuse of an agro-industrial waste of global relevance, with a potential impact on a circular economy model, so the increase of the electrode area (scaling up from powder to larger area sheets), improvement of the impregnation methodology to achieve better dispersion of metallic nanoparticles and improve the functionalization of biochar for these applications, studying new ways of assembling these electrocatalysts in commercial electrolytic cells, will be evaluated in the future.

4 Conclusions

In summary, this article presents the high electrocatalytic performance of Mo/Co electrocatalyst supported on BC derived from residual hazelnut shells. The

Table 1 Different electrocatalysts reported in the literature, based on non-noble metals and the use of BC as the support

Catalyst	Biomass	Surface area ($m^2\ g^{-1}$)	Reaction	Overpotential (V, η_{10})	Tafel slope ($mV\ dec^{-1}$)	References
BC-Mo/Co	Hazelnut shells	321	HER	0.257	51	This work
			OER	0.371	59	
Co@NC nanocages/HCF_{200}	Chinese parasol trees	138	HER	0.261	109	Zhu et al. (2023)
			OER	0.396	90	
Sulfur self-doped	Camelia japonica flowers	–	HER	0.154	89	Xia et al. (2022)
			OER	0.362	86	
MoS_2/NiOOH	Willow catkins	71	HER	0.250	51	Zou et al. (2020)
			OER	0.280	96	
Cobalt	Cotton fibers	–	HER	0.140	48	Jiang et al. (2022)
			OER	0.330	74	
Ni-$CoSe_2$	*Juncus roemerianus*	59	HER	0.250	69	Yang et al. (2022)
			OER	0.325	58	
N-doped biochar/Ni–Fe	Furfural and indole	37.8	HER	0.297	124	Kalusulingam et al. (2024)
			OER	0.300	146	
Co nanoparticles	*Roystonea regia*	1104	HER	0.172	75	Zhou et al. (2024)
			OER	0.320	57	
Cobalt	Lignin	511.4	HER	0.200	94	Li et al. (2024)
			OER	0.331	65	
MoO_3/AC	Human Hair	–	HER	0.353	124	Sekar et al. (2024)
			OER	0.280	35	
$CuCo_2O_4$	*Sargassum Tenerrimum*	–	HER	0.383	100	Attokkaran et al. (2024)
			OER	0.381	44	
Carbon nanosheets	*Neofavolus alveolaris*	8.28	HER	0.447	89	Hareesha et al. (2024)
			OER	0.305	75	

one-step impregnation with KOH and urea enabled the 3D carbon structure production with interconnected hierarchical pores, providing channels for mass transport and a high surface area of 1102 $m^2\ g^{-1}$, an I_D/I_G ratio of 1.08, as well as the presence of graphitic nitrogen. Additionally, the formation of bimetallic Mo/Co active sites was identified, where the combined functionalization of these metals was more effective in reducing the overpotential for HER/OER, as compared to their single use. The overpotentials (η_{10}) achieved by BC-Mo/Co were 0.257 V for HER and 0.370 V for OER in an alkaline medium, with enhanced exposure to active sites and high stability. This research provides valuable insights for electrocatalyst development supported on biomass-derived structures, laying the foundations for scaling up this sustainable material and evaluating its use in electrolytic cells with larger working areas.

Supplementary Information

The online version contains supplementary material available at https://doi.org/10.1007/s42773-025-00464-0.

Additional file 1

Acknowledgements
The authors thank Waste management and Bioenergy Center (University of La Frontera, Chile) for physical-Chemical and morphological analysis, and Centres Científics i Tecnològics (CCiTUB), Universitat de Barcelona, for the expert and technical help on XPS, XRD, and Raman techniques. We also thank the Scientific and Technological Bioresource Nucleus of Universidad de La Frontera (BIOREN–UFRO) and project Service Management Analytical Research and Training Center (SmartC-BIOREN) No. CCSS210005.

Author contributions
JÑ: investigation, data curation, editing, writing. TA and IS: resources, methodology, funding acquisition, review. AR: conceptualization, supervision, methodology. BN and KG: data analysis. GV: computational study. MG: supervision, conceptualization, editing, methodology. MC: review. The author(s) read and approved the final manuscript.

Funding
The authors gratefully acknowledge support through projects ANID scholarship N° 21211437 and FONDECYT Nº 11180752 (Chile), PID2022–138491OB-C33, PID2022-140378OB-I00 and TED2021-130461B-I00 funded by MICIU/AEI/https://doi.org/10.13039/501100011033 (Spain), ERDF/EU and NextGenerationEU/PRTR.

Data availability
The datasets used or analyzed during the current study are available from the corresponding author upon reasonable request.

Declarations

Competing interests

The authors have no competing interests to declare that are relevant to the content of this article.

Author details

[1]Doctoral Program in Engineering Sciences with Specialization in Bioprocesses, University of La Frontera, Av. Francisco Salazar 01145, Temuco, Chile. [2]Departament de Ciència de Materials i Química Física, Secció de Química Física, Facultat de Química, Universitat de Barcelona, Martí i Franquès, 1-11, 08028 Barcelona, Spain. [3]Department of Chemical Sciences and Natural Resources, Faculty of Engineering and Sciences, University of La Frontera, Av. Francisco Salazar 01145, 4780000 Temuco, Chile. [4]Department of Chemical Engineering, University of La Frontera, Av. Francisco Salazar 01145, 4780000 Temuco, Chile. [5]Scientific and Technological Bioresource Nucleus (BIOREN-UFRO), Universidad de La Frontera, Av. Francisco Salazar 01145, 4780000 Temuco, Chile.

Received: 18 November 2024 Revised: 28 March 2025 Accepted: 5 April 2025
Published online: 12 May 2025

References

Abdolahi B, Gholivand MB, Shamsipur M, Amiri M (2021) Engineering of nickel-cobalt oxide nanostructures based on biomass material for high performance supercapacitor and catalytic water splitting. Int J Energy Res 45(9):12879–12897. https://doi.org/10.1002/ER.6618

Almazán-Sánchez PT, Castañeda-Juárez M, Martínez-Miranda V, Solache-Ríos MJ, Lugo-Lugo V, Linares-Hernández I (2015) Behavior of TOC and color in the presence of iron-modified activated carbon in methyl methacrylate wastewater in batch and column systems. Water Air Soil Pollut 226(3):1–13. https://doi.org/10.1007/S11270-015-2302-0

Anantharaj S, Noda S (2022) How properly are we interpreting the Tafel lines in energy conversion electrocatalysis? Mater Today Energy 29:101123. https://doi.org/10.1016/J.MTENER.2022.101123

Anantharaj S, Ede SR, Karthick K, Sam Sankar S, Sangeetha K, Karthik PE, Kundu S (2018) Precision and correctness in the evaluation of electrocatalytic water splitting: revisiting activity parameters with a critical assessment. Energy Environ Sci 11(4):744–771. https://doi.org/10.1039/C7EE03457A

Anantharaj S, Karthik PE, Noda S (2021) The significance of properly reporting turnover frequency in electrocatalysis research. Angew Chem Int Ed 60(43):23051–23067. https://doi.org/10.1002/ANIE.202110352

Attokkaran JR, Beere HK, Samage A, Maraddi AS, Ghosh D, Nataraj SK (2024) Deep eutectic solvent-mediated synthesis of $CuCo_2O_4$ @ *Sargassum tenerrimum* derived carbon heterostructure as an efficient electrocatalyst for oxygen and hydrogen evolution reactions. Int J Hydrogen Energy 93:554–561. https://doi.org/10.1016/J.IJHYDENE.2024.10.360

Bardestani R, Patience GS, Kaliaguine S (2019) Experimental methods in chemical engineering: specific surface area and pore size distribution measurements—BET, BJH, and DFT. Can J Chem Eng 97(11):2781–2791. https://doi.org/10.1002/CJCE.23632

Béguerie T, Weiss-Hortala E, Nzihou A (2022) Calcium as an innovative and effective catalyst for the synthesis of graphene-like materials from cellulose. Sci Rep 12(1):1–11. https://doi.org/10.1038/s41598-022-25943-3

Bhunia K, Chandra M, Kumar Sharma S, Pradhan D, Kim SJ (2023) A critical review on transition metal phosphide based catalyst for electrochemical hydrogen evolution reaction: Gibbs free energy, composition, stability, and true identity of active site. Coord Chem Rev 478:214956. https://doi.org/10.1016/J.CCR.2022.214956

Ceylan S, Topçu Y (2014) Pyrolysis kinetics of hazelnut husk using thermogravimetric analysis. Biores Technol 156:182–188. https://doi.org/10.1016/J.BIORTECH.2014.01.040

Chang S-Q, Cheng C-C, Cheng P-Y, Huang C-L, Lu S-Y (2022) Pulse electrodeposited FeCoNiMnW high entropy alloys as efficient and stable bifunctional electrocatalysts for acidic water splitting. Chem Eng J 446:137452. https://doi.org/10.1016/J.CEJ.2022.137452

Chen C, Sun K, Huang C, Yang M, Fan M, Wang A, Zhang G, Li B, Jiang J, Xu W, Liu J (2023) Investigation on the mechanism of structural reconstruction of biochars derived from lignin and cellulose during graphitization under high temperature. Biochar 5(1):1–14. https://doi.org/10.1007/S42773-023-00229-7

Cheng W, Zhang H, Zhao X, Su H, Tang F, Tian J, Liu Q (2018) A metal-vacancy-solid-solution NiAlP nanowall array bifunctional electrocatalyst for exceptional all-pH overall water splitting. J Mater Chem A 6(20):9420–9427. https://doi.org/10.1039/C8TA01662C

Cui S, Li M, Bo X (2020) Co/Mo_2C composites for efficient hydrogen and oxygen evolution reaction. Int J Hydrogen Energy 45(41):21221–21231. https://doi.org/10.1016/J.IJHYDENE.2020.05.006

Dehkhoda AM, Gyenge E, Ellis N (2016) A novel method to tailor the porous structure of KOH-activated biochar and its application in capacitive deionization and energy storage. Biomass Bioenerg 87:107–121. https://doi.org/10.1016/J.BIOMBIOE.2016.02.023

Deng L, Zhang Y, Wang Y, Yuan H, Chen Y, Wu Y (2021) In situ N-, P- and Ca-codoped biochar derived from animal bones to boost the electrocatalytic hydrogen evolution reaction. Resour Conserv Recycl 170:105568. https://doi.org/10.1016/J.RESCONREC.2021.105568

Dogan A, Siyakus G, Severcan F (2007) FTIR spectroscopic characterization of irradiated hazelnut (*Corylus avellana* L.). Food Chem 100(3):1106–1114. https://doi.org/10.1016/J.FOODCHEM.2005.11.017

Dong Z, Zheng K, Zhang C, Li J, Xie H, Xu C (2023) Modulating the electronic structure of Co in $Co\text{-}Co_8Mo_6C_2$ for effective oxygen evolution reaction. Energy Fuels 37(8):6025–6035. https://doi.org/10.1021/ACS.ENERGYFUELS.2C04151

Duran P, Barra PJ, de la Luz Mora M, Nunes-Nesi A, Merino-Gergichevich C (2022) Boron and zinc diminish grey necrosis incidence by the promotion of desirable microorganisms on hazelnut orchards. Agronomy 12(4):868. https://doi.org/10.3390/AGRONOMY12040868

Fahmy TYA, Fahmy Y, Mobarak F, El-Sakhawy M, Abou-Zeid RE (2020) Biomass pyrolysis: past, present, and future. Environ Dev Sustain 22(1):17–32. https://doi.org/10.1007/S10668-018-0200-5

Gabhi R, Basile L, Kirk DW, Giorcelli M, Tagliaferro A, Jia CQ (2020) Electrical conductivity of wood biochar monoliths and its dependence on pyrolysis temperature. Biochar 2(3):369–378. https://doi.org/10.1007/S42773-020-00056-0

García-Rocha R, Durón-Torres SM, Palomares-Sánchez SA, Del Rio-De Santiago A, Rojas-de Soto I, Escalante-García IL (2023) Effects of heat treatment on the physicochemical properties and electrochemical behavior of biochars for electrocatalyst support applications. Materials 16(16):5571. https://doi.org/10.3390/MA16165571

Ge R, Huo J, Li Y, Liao T, Zhang J, Zhu M, Ahamad T, Li S, Liu H, Feng L, Li W (2022) Electrocatalyst nanoarchitectonics with molybdenum-cobalt bimetallic alloy encapsulated in nitrogen-doped carbon for water splitting reaction. J Alloy Compd 904:164084. https://doi.org/10.1016/J.JALLCOM.2022.164084

Guo R, Yan L, Rao P, Wang R, Guo X (2020a) Nitrogen and sulfur co-doped biochar derived from peanut shell with enhanced adsorption capacity for diethyl phthalate. Environ Pollut 258:113674. https://doi.org/10.1016/J.ENVPOL.2019.113674

Guo T, Zhang X, Liu T, Wu Z, Wang D (2020b) N, K Co-activated biochar-derived molybdenum carbide as efficient electrocatalysts for hydrogen evolution. Appl Surf Sci 509:144879. https://doi.org/10.1016/J.APSUSC.2019.144879

Guo W, Chai DF, Li J, Yang X, Fu S, Sui G, Zhuang Y, Guo D (2024) Strain engineering for electrocatalytic overall water splitting. ChemPlusChem 89(7):e202300605. https://doi.org/10.1002/CPLU.202300605

Han Y, Li P, Tian Z, Zhang C, Ye Y, Zhu X, Liang C (2019) Molybdenum-doped porous cobalt phosphide nanosheets for efficient alkaline hydrogen evolution. ACS Appl Energy Mater 2(9):6302–6310. https://doi.org/10.1021/acsaem.9B00924

Hareesha N, Soumya DM, Mounesh, Manjunatha JG, Rohit RN, Manikanta P, Varun DN, Ataollahi N, Thippeswamy BA, Pramoda K, Nagaraja BM (2024) Honeycomb polypore biomass-derived activated porous carbon nanosheets/graphite/nafion composite: green and sensitive electrocatalyst for nanomolar detection of Hg^{2+} ions and water-splitting reactions. J Environ Chem Eng 12(5):113584. https://doi.org/10.1016/J.JECE.2024.113584

Hou G, Wu J, Li T, Lin J, Wang B, Peng L, Yan T, Hao L, Qiao L, Wu X (2022) Nitrogen-rich biomass derived three-dimensional porous structure

captures FeNi metal nanospheres: an effective electrocatalyst for oxygen evolution reaction. Int J Hydrogen Energy 47(25):12487–12499. https://doi.org/10.1016/J.IJHYDENE.2022.02.004
Jagadeesh N, Sundaram B (2023) Adsorption of pollutants from wastewater by biochar: a review. J Hazard Mater Adv 9:100226. https://doi.org/10.1016/J.HAZADV.2022.100226
Jiang J, Liu Q, Zeng C, Ai L (2017) Cobalt/molybdenum carbide@N-doped carbon as a bifunctional electrocatalyst for hydrogen and oxygen evolution reactions. J Mater Chem A 5(32):16929–16935. https://doi.org/10.1039/C7TA04893A
Jiang E, Song N, Hong S, Xiao M, Zhu D, Yan Z, Sun J, Chen G, Li C, Dong H (2022) Cobalt supported on biomass carbon tubes derived from cotton fibers towards high-efficient electrocatalytic overall water-splitting. Electrochim Acta 407:139895. https://doi.org/10.1016/J.ELECTACTA.2022.139895
Kalusulingam R, Ravi K, Mathi S, Yadhav N, Mikheykin AS, Biradar AV, Srinivasan K, Myasoedova TN (2024) Bimetallic Ni–Fe nanoparticles encapsulated with biomass-derived N-doped graphitic carbon core-shell nanostructures an efficient bifunctional electrocatalyst for enhanced overall seawater splitting and human urine electrolysis. Mater Today Sustain 27:100864. https://doi.org/10.1016/J.MTSUST.2024.100864
Karmakar A, Kundu S (2023) A concise perspective on the effect of interpreting the double layer capacitance data over the intrinsic evaluation parameters in oxygen evolution reaction. Mater Today Energy 33:101259. https://doi.org/10.1016/J.MTENER.2023.101259
Karmaker AK, Rahman MM, Hossain MA, Ahmed MR (2020) Exploration and corrective measures of greenhouse gas emission from fossil fuel power stations for Bangladesh. J Clean Prod 244:118645. https://doi.org/10.1016/J.JCLEPRO.2019.118645
Kiciński W, Dyjak S (2020) Transition metal impurities in carbon-based materials: pitfalls, artifacts and deleterious effects. Carbon 168:748–845. https://doi.org/10.1016/J.CARBON.2020.06.004
Kober T, Schiffer HW, Densing M, Panos E (2020) Global energy perspectives to 2060—WEC's World Energy Scenarios 2019. Energ Strat Rev 31:100523. https://doi.org/10.1016/J.ESR.2020.100523
Król K, Gantner M (2020) Morphological traits and chemical composition of hazelnut from different geographical origins: a review. Agriculture 10(9):375. https://doi.org/10.3390/AGRICULTURE10090375
Lazanas AC, Prodromidis MI (2023) Electrochemical impedance spectroscopy—a tutorial. ACS Meas Sci Au 3(3):162–193. https://doi.org/10.1021/ACSMEASURESCIAU.2C00070
Li L, Wang P, Shao Q, Huang X (2020) Metallic nanostructures with low dimensionality for electrochemical water splitting. Chem Soc Rev 49(10):3072–3106. https://doi.org/10.1039/D0CS00013B
Li L, Cao X, Huo J, Qu J, Chen W, Liu C, Zhao Y, Liu H, Wang G (2023) High valence metals engineering strategies of Fe/Co/Ni-based catalysts for boosted OER electrocatalysis. J Energy Chem 76:195–213. https://doi.org/10.1016/J.JECHEM.2022.09.022
Li G, Zhang Y, Ma W, Liu F, Li H (2024) Oriented construction of lignin-derived carbon hybrid electrocatalyst with superwettable surface and Co-based heterostructure for overall water splitting. Microporous Mesoporous Mater 379:113302. https://doi.org/10.1016/J.MICROMESO.2024.113302
Liang J, Li H, Chen L, Ren M, Fakayode OA, Han J, Zhou C (2023) Efficient hydrogen evolution reaction performance using lignin-assisted chestnut shell carbon-loaded molybdenum disulfide. Ind Crops Prod 193:116214. https://doi.org/10.1016/J.INDCROP.2022.116214
Liu X, Licht G, Licht S (2021) The green synthesis of exceptional braided, helical carbon nanotubes and nanospiral platelets made directly from CO_2. Mater Today Chem 22:100529. https://doi.org/10.1016/J.MTCHEM.2021.100529
Mashamaite CV, Motsi H, Manyevere A, Poswa SB (2024) Assessing the potential of biochar as a viable alternative to synthetic fertilizers in sub-Saharan Africa smallholder farming: a review. Agronomy 14(6):1215. https://doi.org/10.3390/AGRONOMY14061215
Mittal Y, Srivastava P, Kumar N, Kumar M, Singh SK, Martinez F, Yadav AK (2023) Ultra-fast and low-cost electroactive biochar production for electro-active-constructed wetland applications: a circular concept for plant biomass utilization. Chem Eng J 452:138587. https://doi.org/10.1016/J.CEJ.2022.138587
Mu X, Gong L, Yang G, Xiong Y, Wan J, Zhu J, Li R (2022) Biomass-based transition metal phosphides supported on carbon matrix as efficient and stable electrocatalyst for hydrogen evolution reaction. Int J Energy Res 46(3):3502–3511. https://doi.org/10.1002/ER.7400
Nazari M, Ghaemmaghami M (2023) Approach to evaluation of electrocatalytic water splitting parameters, reflecting intrinsic activity: toward the right pathway. Chemsuschem 16(11):e202202126. https://doi.org/10.1002/CSSC.202202126
Neeli ST, Ramsurn H (2018) Synthesis and formation mechanism of iron nanoparticles in graphitized carbon matrices using biochar from biomass model compounds as a support. Carbon 134:480–490. https://doi.org/10.1016/J.CARBON.2018.03.079
Nguyen TB, Sherpa K, Bui XT, Nguyen VT, Vo TDH, Ho HTT, Chen CW, Dong CD (2023) Biochar for soil remediation: a comprehensive review of current research on pollutant removal. Environ Pollut 337:122571. https://doi.org/10.1016/J.ENVPOL.2023.122571
Nguyen VT, Cho K, Choi Y, Hwang B, Park YK, Nam H, Lee D (2024) Biomass-derived materials for energy storage and electrocatalysis: recent advances and future perspectives. Biochar 6(1):1–30. https://doi.org/10.1007/S42773-024-00388-1
Park S, Kim J, Kwon K (2022) A review on biomass-derived N-doped carbons as electrocatalysts in electrochemical energy applications. Chem Eng J 446:137116. https://doi.org/10.1016/J.CEJ.2022.137116
Pereira Lopes R, Astruc D (2021) Biochar as a support for nanocatalysts and other reagents: recent advances and applications. Coord Chem Rev 426:213585. https://doi.org/10.1016/J.CCR.2020.213585
Pingkuo L, Yi G (2019) Graphene's potential in the future industrial development of China. Resour Policy 61:118–127. https://doi.org/10.1016/J.RESOURPOL.2019.02.007
Qu J, Wang Y, Tian X, Jiang Z, Deng F, Tao Y, Jiang Q, Wang L, Zhang Y (2021) KOH-activated porous biochar with high specific surface area for adsorptive removal of chromium(VI) and naphthalene from water: affecting factors, mechanisms and reusability exploration. J Hazard Mater 401:123292. https://doi.org/10.1016/J.JHAZMAT.2020.123292
Romero Millán LM, Ghogia AC, White CE, Nzihou A (2023) Iron nanoparticles to catalyze graphitization of cellulose for energy storage applications. ACS Appl Nano Mater 6(5):3549–3559. https://doi.org/10.1021/ACSANM.2C05312
Sagues WJ, Yang J, Monroe N, Han SD, Vinzant T, Yung M, Jameel H, Nimlos M, Park S (2020) A simple method for producing bio-based anode materials for lithium-ion batteries. Green Chem 22(20):7093–7108. https://doi.org/10.1039/D0GC02286A
Sakhiya AK, Anand A, Kaushal P (2020) Production, activation, and applications of biochar in recent times. Biochar 2(3):253–285. https://doi.org/10.1007/S42773-020-00047-1
Sarangi PK, Nanda S (2020) Biohydrogen production through dark fermentation. Chem Eng Technol 43(4):601–612. https://doi.org/10.1002/CEAT.201900452
Sekar S, Yun JS, Park S, Kim DY, Lee Y, Lee S (2024) Excellent bifunctional water electrolysis activities of α-MoO_3/AC nanocomposites. Int J Energy Res 2024(1):3167699. https://doi.org/10.1155/2024/3167699
Şencan A, Karaboyacı M, Kılıç M (2015) Determination of lead(II) sorption capacity of hazelnut shell and activated carbon obtained from hazelnut shell activated with $ZnCl_2$. Environ Sci Pollut Res 22(5):3238–3248. https://doi.org/10.1007/S11356-014-2974-9
Shinagawa T, Garcia-Esparza AT, Takanabe K (2015) Insight on Tafel slopes from a microkinetic analysis of aqueous electrocatalysis for energy conversion. Sci Rep 5(1):1–21. https://doi.org/10.1038/SREP13801
Singh A, Sharma R, Pant D, Malaviya P (2021) Engineered algal biochar for contaminant remediation and electrochemical applications. Sci Total Environ 774:145676. https://doi.org/10.1016/J.SCITOTENV.2021.145676
Söyler N, Ceylan S (2021) Thermokinetic analysis and product characterization of waste tire-hazelnut shell co-pyrolysis: TG-FTIR and fixed bed reactor study. J Environ Chem Eng 9(5):106165. https://doi.org/10.1016/J.JECE.2021.106165
Tian B, Mao S, Guo F, Bai J, Shu R, Qian L, Liu Q (2022) Monolithic biochar-supported cobalt-based catalysts with high-activity and superior-stability for biomass tar reforming. Energy 242:122970. https://doi.org/10.1016/J.ENERGY.2021.122970
Tsubota T, Tsuchiya S, Kusumoto T, Kalderis D (2021) Assessment of biochar produced by flame-curtain pyrolysis as a precursor for the development of an efficient electric double-layer capacitor. Energies 14(22):7671. https://doi.org/10.3390/EN14227671

Tüysüz H (2023) Alkaline water electrolysis for green hydrogen production. Acc Chem Res 57:7. https://doi.org/10.1021/ACS.ACCOUNTS.3C00709

Velazquez Abad A, Dodds PE (2020) Green hydrogen characterisation initiatives: definitions, standards, guarantees of origin, and challenges. Energy Policy 138:111300. https://doi.org/10.1016/J.ENPOL.2020.111300

Wang Q, Hu W, Huang Y (2017) Nitrogen doped graphene anchored cobalt oxides efficiently bi-functionally catalyze both oxygen reduction reaction and oxygen revolution reaction. Int J Hydrogen Energy 42(9):5899–5907. https://doi.org/10.1016/J.IJHYDENE.2017.02.038

Xia C, Surendran S, Ji S, Kim D, Chae Y, Kim J, Je M, Han MK, Choe WS, Choi CH, Choi H, Kim JK, Sim U (2022) A sulfur self-doped multifunctional biochar catalyst for overall water splitting and a supercapacitor from *Camellia japonica* flowers. Carbon Energy 4(4):491–505. https://doi.org/10.1002/CEY2.207

Xiao X, Li Z, Xiong Y, Yang YW (2023) IrMo nanocluster-doped porous carbon electrocatalysts derived from cucurbit[6]uril boost efficient alkaline hydrogen evolution. J Am Chem Soc 145(30):16548–16556. https://doi.org/10.1021/JACS.3C03489

Xu X, Zhao B, Sun M, Chen X, Zhang M, Li H, Xu S (2017) Co-pyrolysis characteristics of municipal sewage sludge and hazelnut shell by TG-DTG-MS and residue analysis. Waste Manage 62:91–100. https://doi.org/10.1016/J.WASMAN.2017.02.012

Xu J, Liu J, Ling P, Zhang X, Xu K, He L, Wang Y, Su S, Hu S, Xiang J (2020) Raman spectroscopy of biochar from the pyrolysis of three typical Chinese biomasses: a novel method for rapidly evaluating the biochar property. Energy 202:117644. https://doi.org/10.1016/J.ENERGY.2020.117644

Xu C, Hong Y, Li Z, Di X, Wang W, Dong X, Mou X (2025) Transition metal-based heterojunctions for alkaline electrocatalytic water splitting. Coord Chem Rev 523:216287. https://doi.org/10.1016/J.CCR.2024.216287

Yang G, Zhang Y, Liu J, Wang M, Gu C, Li J (2022) In-situ growth of Ni–$CoSe_2$ on biomass-derived carbon tubes as an efficient electrocatalyst for overall water splitting. Int J Hydrogen Energy 47(92):38920–38929. https://doi.org/10.1016/J.IJHYDENE.2022.09.067

Yaseen W, Xie M, Yusuf BA, Xu Y, Ullah N, Rafiq M, Ali A, Xie J (2022) Synergistically coupling of Co/Mo_2C/$Co_6Mo_6C_2$@C electrocatalyst for overall water splitting: the role of carbon precursors in structural engineering and catalytic activity. Appl Surf Sci 579:152148. https://doi.org/10.1016/J.APSUSC.2021.152148

Zhang H, Zhang M, Zhang H, Yu T, Qu C (2023) Recent development of sludge biochar-based catalysts in advanced oxidation processes for removing wastewater contaminants: a review. Fuel 348:128444. https://doi.org/10.1016/J.FUEL.2023.128444

Zhou Y, Luo Y, Li Q, Liang J, Liu F, Cai Y, Lin L, Wu Q, Li K (2024) Cobalt nanoparticles encapsulated in the biomass-derived carbon: an efficient and bifunctional electrocatalyst for overall water splitting. Energy Fuels 38(16):15560–15570. https://doi.org/10.1021/ACS.ENERGYFUELS.4C01798

Zhu J, Hu L, Zhao P, Lee LYS, Wong KY (2020) Recent advances in electrocatalytic hydrogen evolution using nanoparticles. Chem Rev 120(2):851–918. https://doi.org/10.1021/acs.chemrev.9b00248

Zhu D, Shao J, Li Z, Yang H, Zhang S, Chen H (2021) Nano nickel embedded in N-doped CNTs-supported porous biochar for adsorption-reduction of hexavalent chromium. J Hazard Mater 416:125693. https://doi.org/10.1016/J.JHAZMAT.2021.125693

Zhu R, Yu X, Li W, Li M, Bo X, Gan G (2023) Cobalt nanoparticles-embedded porous carbon nanocages uniformly dispersed hollow carbon fibers as the accelerated electrocatalysts toward water splitting. J Alloy Compd 947:169488. https://doi.org/10.1016/J.JALLCOM.2023.169488

Zou Y, Xiao B, Shi JW, Hao H, Ma D, Lv Y, Sun G, Li J, Cheng Y (2020) 3D hierarchical heterostructure assembled by NiFe LDH/(NiFe)S_x on biomass-derived hollow carbon microtubes as bifunctional electrocatalysts for overall water splitting. Electrochim Acta 348:136339. https://doi.org/10.1016/J.ELECTACTA.2020.136339